Thermal synthesis of $NiMn_2O_4$ spinel employing Mn oxide ores as starting material

R. S. Nascimento[1], B. A. M. Figueira[2,4]*, E. F. Neto[3], A. A. Rabelo[3], O. J. C. Fernandez[4], P. T. S. da Luz[4], M. L. da Costa[1]

[1]Programa de Pós-graduação em Geologia e Geociências, Universidade Federal do Pará, 66075-110, Belém, PA, Brazil

[2]Programa de Pós-graduação em Ambiente e Qualidade de Vida, Universidade Federal do Oeste do Pará, 68040-255, Santarém, PA, Brazil

[3]Instituto de Geociências e Engenharia, Universidade Federal do Sul e Sudeste do Pará, 68000-500, Marabá, PA, Brazil

[4]Programa de Pós-graduação em Engenharia de Materiais, Instituto Federal do Pará, 66093-020, Belém, PA, Brazil

Abstract

It is described for the first time the synthesis and characterization of $NiMn_2O_4$ employing the Mn ores from the Amazon Region as starting material, instead of using commercial reagents as normally occurs in its synthesis process. Initially, an Mn ore was transformed into a single product, the octahedral layer (OL) manganese oxide with Ni^{2+} ions interlayer (Ni-OL-2), which was used as a matrix to obtain $NiMn_2O_4$ by thermal decomposition. The following techniques were used for characterization: X-ray diffraction (XRD), X-ray fluorescence spectroscopy (XRF), infrared spectroscopy (FTIR), thermal analysis (TG-DTA), scanning (SEM) and transmission (TEM) electron microscopies. The results revealed that Mn oxide ore composed of nsutite mineral transformed into a well-ordered crystalline Ni-OL-2 phase, after the hydrothermal and cation exchange process. The thermal decomposition of Ni-OL-2 produced the nickel manganite phase at 850 °C with spherical ball morphology and crystal sizes in the range of 200-300 nm.

Keywords: Amazon region, Mn oxide ore, synthesis, characterization, $NiMn_2O_4$.

INTRODUCTION

Oxides with a spinel structure constitute an important family of inorganic compounds that have different physical properties, such as magnetic and electrical, which are strongly dependent on the location and oxidation state of the cations present in the crystalline structure [1]. These structures have the general formula AB_2O_4, where the atoms A (divalent cations) and B (trivalent cations) occupy the tetrahedral XO_4 (X= Mg, Fe, Ni, Mn, and Zn) and octahedral sites YO_6 (Y= Al, Fe, Cr, and Mn), forming a face-centered (F) or body-centered (I) cubic structure through O^{2-} ions [2-4]. Among the various compounds, manganese oxides with AMn_2O_4 structure (A= Li, Mg, Fe, Ni, among others) can be highlighted, since they have unique magnetic and electrical properties, with the advantage of not being harmful to the environment as observed with materials such as $LiCo_2O_4$, $NiCo_2O_4$, $FeCo_2O_4$, among others [5]. An important Mn spinel structure is nickel manganite ($NiMn_2O_4$), as it is widely applied in the industry as a basis for ceramic temperature sensors (thermistors), as well as applications in photocatalysis [6-9].

Currently, there are several routes and sources for obtaining $NiMn_2O_4$, because depending on them, this material can be obtained with different physical (film, powder, single crystals, and nanocrystals) and morphological properties [2, 5, 10-12]. Among the synthesis routes, the following can be highlighted: i) sol-gel [13]; ii) hydroxide route [11]; iii) co-precipitation [7]; iv) thermal decomposition [4]; and v) solid-state reaction [1]. Generally, the routes described above are carried out in the laboratory with commercial reagents based on manganese salts such as: $MnSO_4$, $MnCl_2$, $Mn(CH_3COO)_2$, $Mn(NO_3)_2$. To our knowledge, so far there are no studies using natural sources of Mn (ore, tailings, mineral) as a source of this element for the synthesis of $NiMn_2O_4$. Within this context and the technological importance of the material, the objective of this work was to develop a study of synthesis and characterization of $NiMn_2O_4$ from a relatively low-cost raw material, the Mn oxide ore from an important manganese deposit in the Amazon Region.

MATERIAL AND METHODS

Synthesis route: the Mn oxide ore sample employed was collected from the Carajás Mineral Province (Pará, Brazil).

* https://orcid.org/0000-0002-0507-8662

The as-received sample was crushed, pulverized in a planetary ball mill (PM 100, Retsch), and denoted as SN-02. All other reagents used in this work were of analytical grades such as HCl (Vetec, purity >37%), H_2O_2 (Dinamica, purity >35% v/v), NaOH (Neon, purity >99.5%), and $Ni(SO_4)_2.6H_2O$ (Neon, purity >99.9%). The synthesis process started with the dissolution of 1 g of Mn oxide ore (SN-02) in 100 mL of 2.5 mol.L^{-1} HCl at 90 °C/6 h, to release Mn^{2+} ions in an acidic solution. Subsequently, a mixed solution of 1.5 mol.L^{-1} NaOH and 1 mol.L^{-1} H_2O_2 was added, which quickly formed a dark precipitate (sample MnO-PPT). The material was washed with distilled water and dried at 70 °C. For the synthesis of Na-birnessite, hydrothermal treatment of 0.5 g of MnO-PPT in 40 mL of 5.5 mol.L^{-1} of NaOH at 190 °C/24 h was adopted, as described by Cornell and Giovanolli [14]. The final product was washed with deionized water, dried, and coded as Na-MnO-X. Through an ion exchange process, a mass of 1 g sample (Na-MnO-X) was added to a 100 mL of 1 mol.L^{-1} solution of $Ni(SO_4)_2.6H_2O$, for 24 h at room temperature and kept under vigorous agitation. This procedure was used to obtain Ni-buserite (sample Ni-MnO-X), which was thermally treated up to 850 °C for conversion into $NiMn_2O_4$.

Characterization: initially, the mineralogical characterization of the products was carried out using an X-ray diffractometer (XRD, D2 Phaser, Bruker) in a copper tube, with a voltage of 30 kV and 10 mA, and a detection system (LynxEye). For the chemical characterization of the Mn ore, a sequential X-ray fluorescence spectrometer (XRF, Axios Minerals, Panalytical) equipped with an Rh anode X-ray tube was used. The spectroscopic characterization of the products was performed using a molecular absorption spectrometer in the IR region with a Fourier transform (FTIR, Vertex 70, Bruker). The samples were prepared in pressed KBr pellets (0.200 g KBr/0.0013 g sample). Thermogravimetry-differential thermal analysis (TG-DTA) curves were collected in a thermoanalyzer (PL-ST, Thermal Sci.). The analyzes were carried out in a platinum crucible, heating at 10 °C/min with initial and final temperatures of 25 and 1050 °C, respectively. Scanning electron microscopy-energy dispersive spectroscopy (SEM-EDS) studies were performed in a microscope (Leo, Zeiss) using secondary electron images obtained at 20 kV, with a working distance of 11 mm. The morphological characterization by transmission electron microscopy (TEM) was obtained with a microscope (Tecnai G2-20, FEI) with a LaB_6 filament thermionic gun, with an applied voltage of 200 kV, a line resolution of 0.24 nm and point resolution of 0.10 nm (magnifications from 25x to 1100000x).

RESULTS AND DISCUSSION

Characterization of raw material and lamellar products (Na-birnessite and Ni-buserite)

The XRD patterns of the raw material and its synthetic products related to transformation into Na-birnessite (Na-MnO-X) and Ni-buserite (Ni-MnO-X) are shown in Fig. 1. For SN-02 (Fig. 1a), although the XRD pattern presented a low intensity and resolution of the peaks, there was a predominance of them in 22.7°, 37.1°, 42.45°, 56.2°, 62.22°, and 68.77° (2θ), which were characteristic of the planes (120), (131), (300), (160), (421), and (003) of orthorhombic nsutite or its synthetic phase [15-17]. It was not possible to affirm the exclusive presence of nsutite based only on this diffractogram. The chemical composition of SN-02 was investigated by XRF analysis and the data revealed the major presence of manganese (85.84% of MnO), which could be related to nsutite. The manganese content was well correlated with the contents described by Mohapatra et al. [18] and Nimfopoulos and Pattrik [19] of this mineral. The contents of SiO_2 (0.23%), Al_2O_3 (0.47%), Na_2O (0.15%), P_2O_5 (0.09%), and K_2O (0.71%) did not reach 1% by weight. After the chemical processes developed, the Mn ore was initially converted into monoclinic birnessite (Fig. 1b), as indicated by the peaks at 12.27° and 25.12° (2θ) that belong to the basal planes (001) and (002) of the sodic lamellar phase (PDF 043-1456). The calculated interlamellar distance of the (001) plane was 7.20 Å, which after ion exchange treatment between Na^+ ions with hydrated Ni^{2+} cations, expanded to 9.57 Å forming the Ni-buserite phase. This value corroborated the results of the study by Kuma et al. [20], who demonstrated a maximum ion exchange capacity between these cations of 87% and a value of 9.63 Å (~9.65 Å calculated) for Ni-buserite interlamellar distance with hexagonal symmetry. The peaks at 9.35°, 12.41°, 18.54°, 24.93°, and 36.16° (2θ) in the Ni-MnO-X sample (Fig. 1c) belong to the planes (001), ($^2/_3$ 00), (002), (003), (004), and (020) of nickel manganite (PDF 050-0016). As could be seen, the nsutite-rich Mn oxide ore was fully converted to the previously proposed nickel lamellar phase.

A complementary characterization of the products described above was performed by FTIR spectroscopy (Fig. 2). In the range between 1500-400 cm^{-1}, stretching modes of Mn-O bonds of MnO_6 octahedra of tunnel structures and the

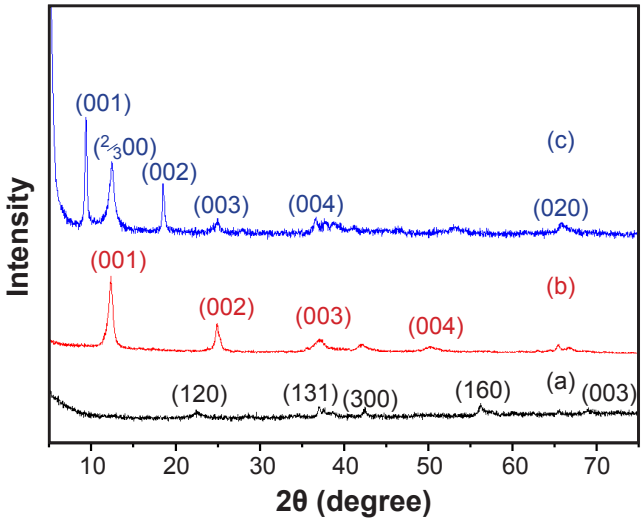

Figure 1: XRD patterns of SN-02 (a), Na-MnO-X (b), and Ni-MnO-X (c).

Mn oxide layer were identified. For example, FTIR bands (SN-02) occurring at 520, 600, and 679 cm^{-1} were assigned to the metal-oxygen vibrational modes of the nsutite tunnel structure [22, 23]. Considering the structure as a tunnel intergrowth of 1x1 MnO_6 (pyrolusite) and 1x2 (ramsdellite) octahedrons, the bands at 520 and 600 cm^{-1} were of ν_6 and ν_7 stretches of Mn-O-Mn vibrational modes in the octahedron site lattice 1x1 (pyrolusite), while the 679 cm^{-1} referred to the ν_8 Mn-O vibrational modes of 1x2 octahedra blocks (ramsdellite). The bands at 1028 and 1395 cm^{-1} have already been identified in mineral characterization studies of nsutite and reinforce the presence of this phase, identified in the XRD pattern of SN-02 with low definition and intensity peaks [18, 24]. The FTIR spectrum of Na-MnO-X was also characterized by vibrational bands of Mn-O-Mn stretches of MnO_6 octahedral chains, but layer-structured Mn oxide. The bands at 410, 473, 510, and 640 cm^{-1} are reported to be ν_3, ν_5, ν_6, and ν_8 vibrational stretches of Mn-O-Mn bonds along the MnO_6 octahedral chains of Na-birnessite [22, 25]. The presence of an intense band at 867 cm^{-1} corresponded to the vibrational modes of Mn-O-H also in the octahedral layers [21]. For the Ni-buserite structure (Ni-MnO-X), Mn-O-Mn stretch vibrations were identified at slightly spaced positions close to 530 and 655 cm^{-1}, as well as vibrational modes of Mn-OH at 910 cm^{-1}. The intense bands at 1024 and 1110 cm^{-1} were assigned to the Mn^{3+}-O stretching, reinforcing the presence of Mn^{3+} cations in the MnO_6 octahedra of the lamellar chains, in addition to Mn^{4+} [21, 25]. The range of 4000-3000 cm^{-1} was used for the spectroscopic characterization of H_2O and OH- species present in the structures. For SN-02, the bands at 3728, 3696, and 3433 cm^{-1} referred to vibrational stretches of hydroxyl groups of crystallizing H_2O molecules adsorbed on the nsutite structure. The bands at 3357 and 3251 cm^{-1} in Na-MnO-X could be assigned to the symmetric (ν_1) and anti-symmetric (ν_3) H-O bonds in water molecules that form a monolayer with Na^+ ions stretches, as well as bands at 3518, 3450, and 3380 cm^{-1} of Ni-MnO-X, with the difference that they refer to the water molecules that make up a double layer around Ni^{2+} ions in the Ni-buserite interlamellar space [26].

Thermal synthesis of $NiMnO_3$ and $NiMn_2O_4$

For the thermal synthesis studies of $NiMnO_3$ and $NiMn_2O_4$ from the Ni-buserite lamellar phase, its thermal behavior was initially investigated through TG-DTA curves, as shown in Fig. 3. Five major endothermic thermal events were identified with a total weight loss of 25.46%. The major weight loss (18.4%) was observed in the temperature range between 25 and 190 °C, which corresponded to the processes of elimination of H_2O molecules and OH- groups from the Ni-buserite lamellar structure. At around 65 °C, the first endothermic event was observed with a weight loss of around 9%, mainly related to the desorption of H_2O molecules without damaging the lamellar structure. The second thermal event (~10.7% in weight loss) referred to the progressive loss of H_2O molecules and OH- groups present between the MnO_6 octahedral sheets with progressive reduction of the space between the layers with increasing temperature. The next two endothermic events were at 620 and 650 °C (~3% weight loss), which were related to the formation of the $NiMn_2O_4$ phase through the intermediate $NiMnO_3$ phase [27]. It is worth mentioning the absence of the endothermic peak related to the conversion of Ni-buserite to $NiMnO_3$, probably due to the experimental conditions used in the thermal analysis.

An X-ray diffractometry monitoring study of Ni-buserite up to 900 °C for 1 h was carried out and the results are presented in three heating ranges (Fig. 4): 25 to 175 °C (thermal decomposition and collapse of Ni-buserite), 200 to 500 °C (crystallization of $NiMnO_3$), and 550 to 900 °C (crystallization of $NiMn_2O_4$). Regarding the data shown in Fig. 4a, in the range of 25 to 75 °C, a slight reduction in the interlamellar space and maintenance of the layered structure

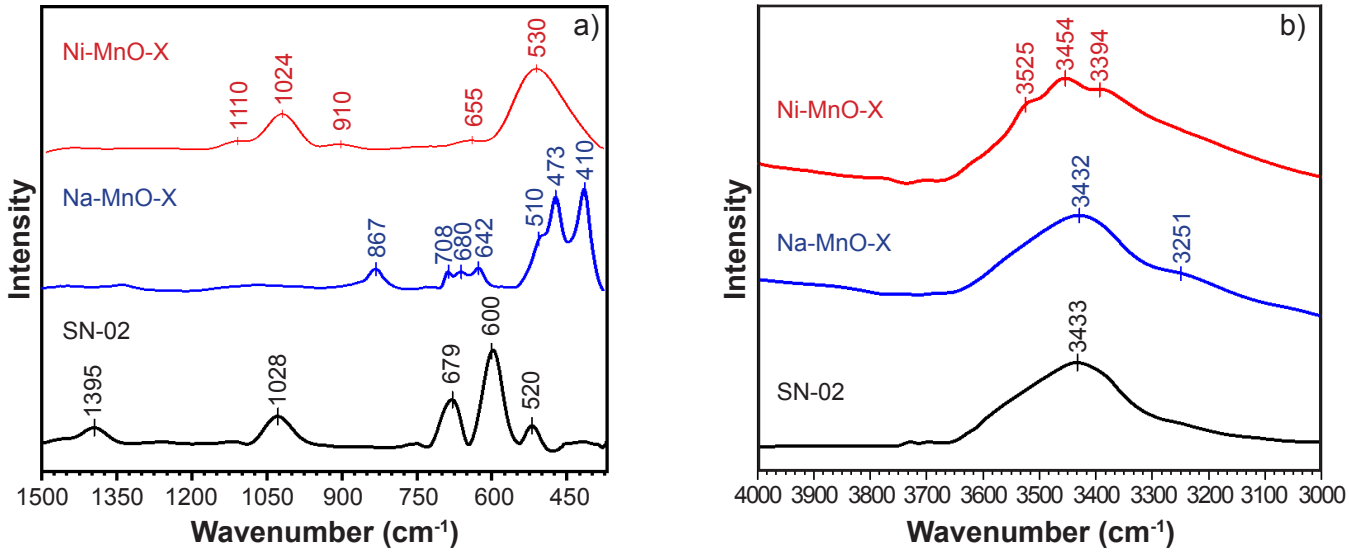

Figure 2: FTIR spectra of SN-02, Na-MnO-X, and Ni-MnO-X in the ranges between 1500-400 cm^{-1} (a) and 4000-3000 cm^{-1} (b).

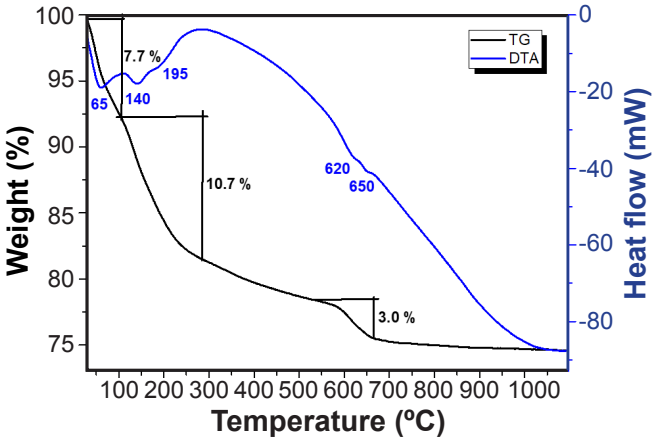

Figure 3: TG-DTA curves of Ni-OL-2 sample.

with 9.55 Å of interlamellar distance could be observed. However, above 100 °C, it reduced to 9.45 Å and only the residual presence of Ni-buserite was identified, as indicated by the plane (001) around 9.35° (2θ). With the increase in temperature up to 175 °C, the Ni-buserite interlamellar space was considerably reduced, as well as broadening and reduction in the intensity of the basal plane at 12.5° (2θ), indicating intense disarrangement of the layered phase. In Fig. 4b, the XRD patterns of the samples heated between 200 and 500 °C showed a complete thermal decomposition of Ni-birnessite through the disappearance of the plane (001) at 300 °C and at the same time, the increasing crystallization of the rhombohedral phase $NiMnO_3$ from 200 °C through the appearance of its main peak at 36.51°. Around 500 °C, the peaks observed at 24.6°, 33.55°, 36.51°, 41.83°, 54.9°, and 65.82° (2θ) were from the planes (110), (211), (1$\bar{1}$0), (210), (311), and (331) of rhombohedral $NiMnO_3$ crystalline phase (PDF 03-065-3695) with no impurities, which corroborated the previous studies of material synthesis by co-precipitation process and hydrothermal treatment, thermal decomposition of Mn salts, and also under hydrothermal synthesis by microwave-assisted radiation [28-30]. The mean crystallite size (Scherrer equation) observed for $NiMnO_3$ was ~225 nm. In order to determine the optimal conditions for obtaining $NiMn_2O_4$ from $NiMnO_3$, an extension of the thermal treatment was carried out up to 850 °C (Fig. 4c). Up to 600 °C, there was still a predominance of $NiMnO_3$, in addition to the Mn_2O_3 phase as observed by the peaks around 33°, 35°, 42°, 55.3°, and 65.9° (2θ). From the XRD patterns of the heated samples between 650 and 850 °C, it could be inferred that at 650 °C, the formation of the cubic phase (Fd-3m) $NiMn_2O_4$ started, although its pure form was obtained only at 850 °C, as indicated by peaks at 18.3°, 30.09°, 35.34°, 36.98°, 42.9°, 56.75°, and 62.32° (2θ), which were related to the planes (111), (220), (311), (222), (400), (511), and (440) of $NiMn_2O_4$ (PDF 36-0083). These results suggested that $NiMn_2O_4$ was not obtained from the direct thermal decomposition of $NiMnO_3$ but probably from a combination of this phase with Mn_2O_3. It is noteworthy that the thermal decomposition process was in accordance with the study by De Vidales et al. [31], but with the synthesis of nickel manganite in a much shorter heating time and without the presence of the intermediate phases γ-MnO_2 and Mn_3O_4 reported by them.

The morphological aspects of the raw material and synthetic products are displayed in Fig. 5. The micrograph of Mn ore (SN-02) revealed an aggregate of globules dispersed on an irregular surface, contrasting to the 'hedgehog-like' and 'layer-cake-like' aspects of its synthetic analog earlier reported [16, 17]. The image of the lamellar product Na-birnessite (Na-MnO-X) obtained by hydrothermal treatment showed the overlapping of sheets with crystal size above 30 μm. The Ni-buserite-type phase (Ni-MnO-X) showed the same plate morphology, suggesting that the ion exchange process did not modify the morphology of the lamellar product. Regarding the morphological aspects of $NiMnO_3$ and $NiMn_2O_4$, it was noted that the increase in temperature

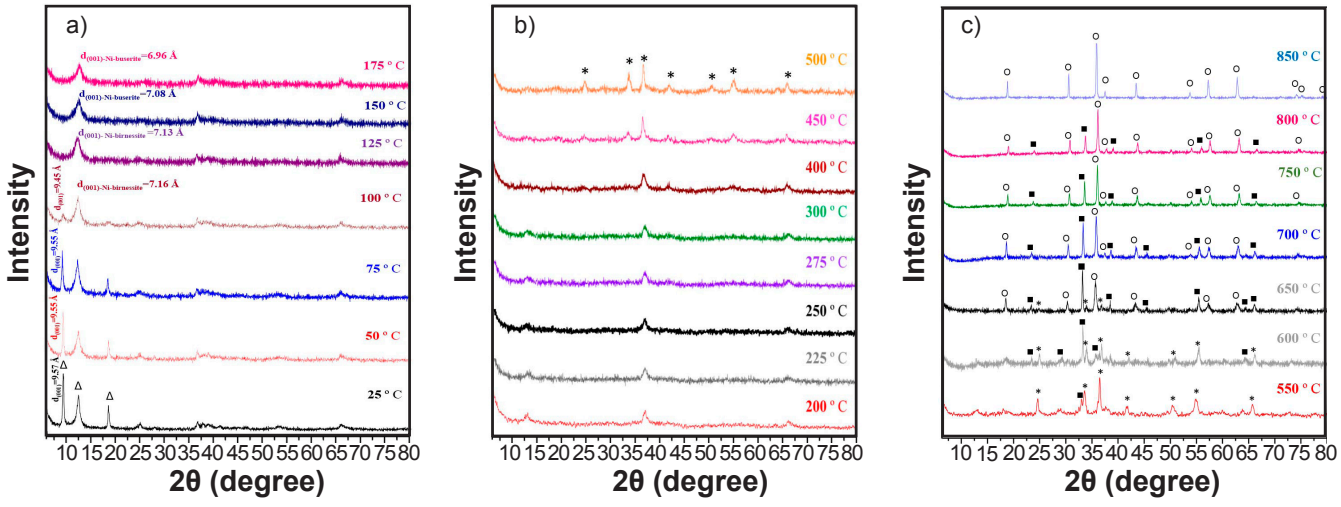

Figure 4: XRD patterns of Ni-buserite heated between 25 and 175 °C (a), 200 and 500 °C (b), and 550 and 850 °C (c). Δ: Ni-buserite; *: $NiMnO_3$; ■: Mn_2O_3; o: $NiMnO_4$.

formed particles with more defined grains; this was clearly visible when comparing micrographs of samples heated at 450 °C (Ni-MnO-X-450 °C) and 850 °C (Ni-MnO-X-850 °C). The material heated at 450 °C showed aggregates with irregular shape and size, and at 850 °C a clear granular aspect was observed, ranging in size below 1 μm. It is noteworthy that these morphologies have already been reported for these materials synthesized by commercial reagents and/or different synthesis routes [1, 10, 11, 32].

Fig. 6 presents the TEM images of the $NiMnO_3$ (Ni-MnO-X-450 °C) and $NiMn_2O_4$ (Ni-MnO-X-850 °C) synthesized products. It was noted that the $NiMnO_3$ sample obtained at 450 °C consisted of unshaped aggregates-like crystals ranging in size from 300-400 nm. When the reaction temperature was enhanced up to 850 °C, the pseudo-hexagonal morphology of $NiMn_2O_4$ particles was formed, suggesting that the structure of the synthesized particles clearly was dependent on the reaction temperature. The dimension of the particles around 100 and 200 nm was compatible with that calculated by the Scherrer equation, decreasing the particle size with an increase in temperature.

Fig. 7 shows the FTIR spectra of Ni-MnO-X-450 °C and Ni-MnO-X-850 °C. In the region of 4000-1500 cm^{-1}; both spectra showed similar bands around 3465 and 1630 cm^{-1} due to H_2O molecules and OH- groups adsorbed on the surface of $NiMnO_3$ and $NiMn_2O_4$ phases, respectively. On the other hand, in the range of 1500-400 cm^{-1}, unique FTIR bands of $NiMnO_3$ were visualized at 525 and 585 cm^{-1} and correlated

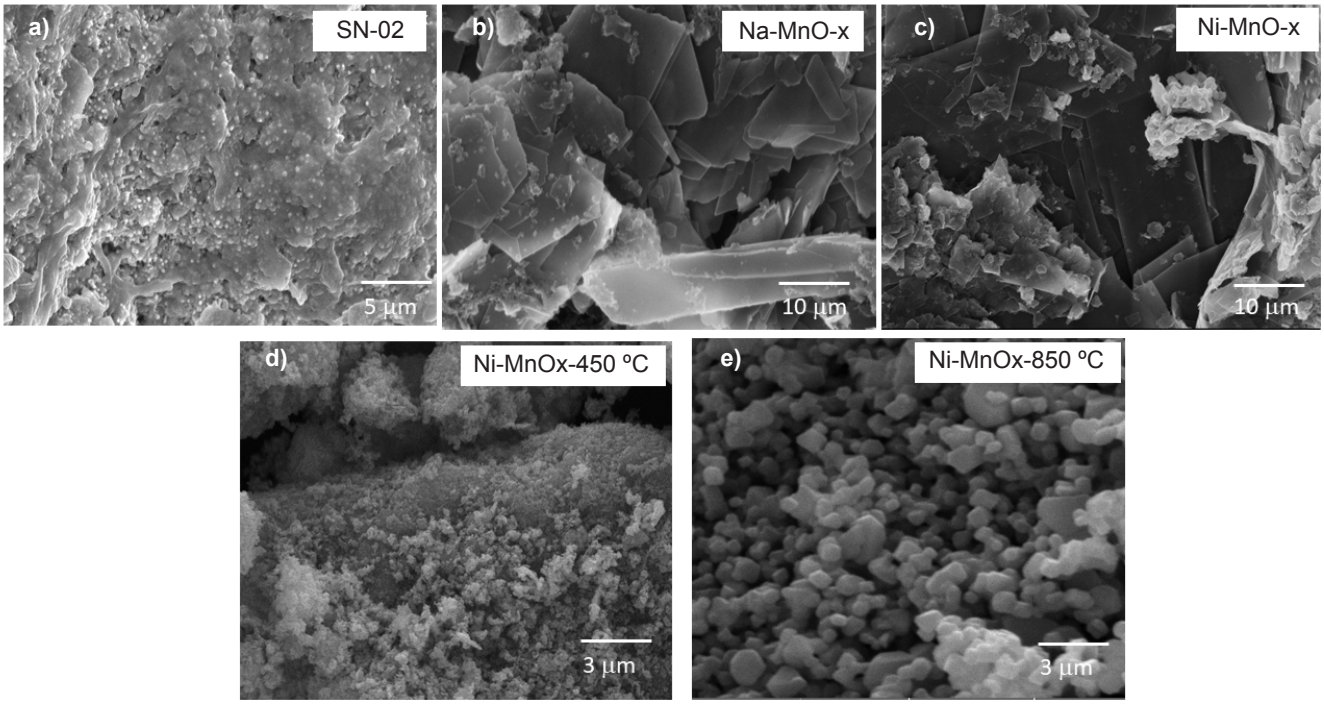

Figure 5: Micrographs generated by SEM of SN-02 (a), Na-MnO-X (b), Ni-MnO-X (c), Ni-MnO-X-450 °C (d), and Ni-MnO-X-850 °C (e) products.

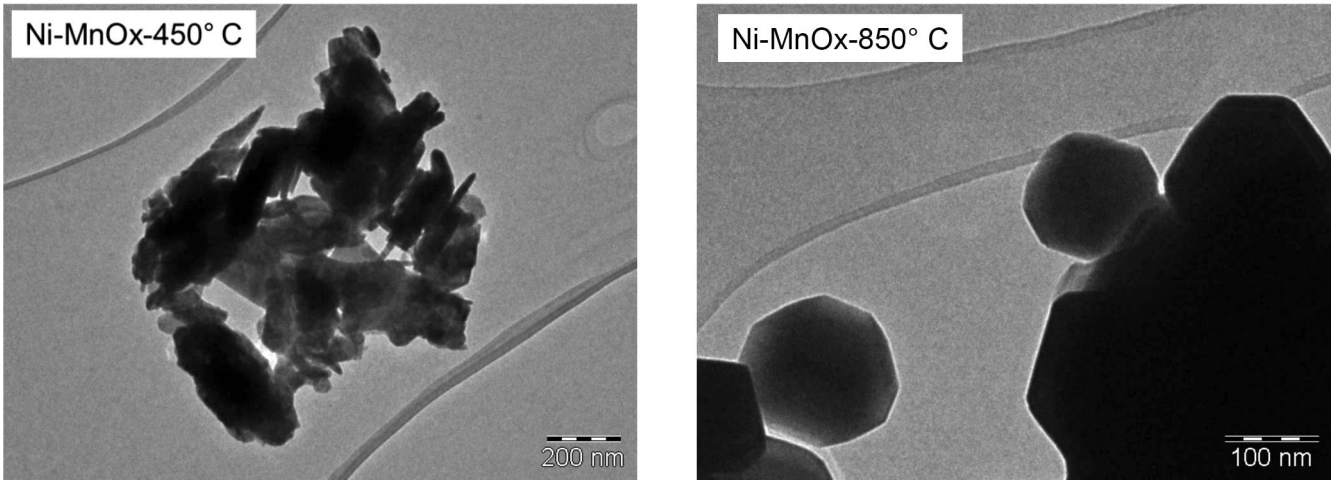

Figure 6: Images obtained by TEM analysis of the thermally synthesized products Ni-MnO-X-450 °C (a) and Ni-MnO-X-850 °C (b).

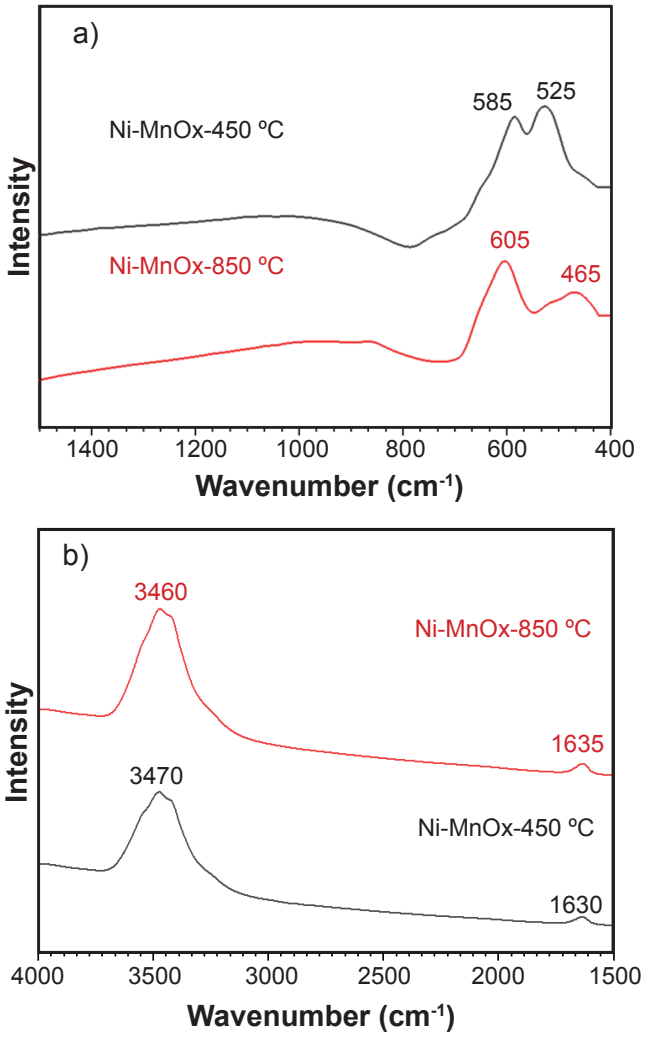

Figure 7: FTIR spectra of Ni-MnO-X-450 °C and Ni-MnO-X-850 °C materials in the ranges between 1500-400 cm^{-1} (a) and 4000-1500 cm^{-1} (b).

to stretches of Ni-O and Mn-O bonds in the octahedra of the ilmenite structure [29, 33], whereas the bands at 605 and 465 cm^{-1} were assigned to the stretches of metal-oxygen bonds of tetrahedral $(Mn/Ni)O_4$ and octahedral $(Mn/Ni)O_6$ units of the spinel structure $NiMn_2O_4$ [33-35]. The absence of other bands suggested the purity of the materials.

CONCLUSIONS

The transformation of natural sources such as Mn oxide ore from the Mineral Province of Carajás (Brazil) into $NiMn_2O_4$-type material was proposed. Firstly, the Mn source was converted into Ni-buserite-type octahedral layer manganese oxide, which showed platelet morphology and thermal stability below 300 °C. With the increase in temperature up to 500 °C, buserite converted into $NiMnO_3$-type phase with grains without defined morphology and average size between 200 and 300 nm. After thermal treatment above 850 °C, well-crystallized $NiMn_2O_4$, with globule grains and size of grains close to those of $NiMnO_3$ could be obtained. The purity of the products was confirmed by X-ray diffractometry, FTIR spectroscopy, and microscopic analysis by SEM and TEM, thus showing that Mn oxide ore could be an interesting, abundant, and low-cost source for the production of materials of great relevance to modern technology.

ACKNOWLEDGMENTS

The authors are grateful for the financial-technical supports of the CNPQ, CAPES, CETENE, and LCM (UFPA).

REFERENCES

[1] P.N. Lisboa-Filho, M. Bahout, P. Barahona, C. Moure, O. Peña, J. Phys. Chem. Solids **66** (2005) 1206.
[2] S. Åsbrink, A. Waśkowska, M. Drozd, E. Talik, J. Phys. Chem. Solids **58** (1997) 725.
[3] S. Azazza, Y. Song, M. Bououdina, in "CRC concise encyclopedia of nanotechnology", B.I. Kharisov, O.V. Kharissova, U. Oritz-Mendez (Eds.), CRC Press (2015) 996.
[4] P.N. Lisboa-Filho, C. Vila, M.S. Góes, C. Morilla-Santos, L. Gama, E. Longo, C.O. Paiva-Santos, Mater. Chem. Phys. **85** (2004) 377.
[5] S.A. Hosseini, A. Niaei, D. Salari, S.R. Nabavi, Ceram. Int. **38** (2012) 1655.
[6] A. Díez, R. Schimidt, A.E. Sagua, M.A. Frechero, E. Matesanz, C. Leon, E. Morán, J. Eur. Ceram. Soc. **30** (2010) 2617.
[7] R. Schmidt, A. Stiegelschmitt, A. Roosen, A.W. Brinkman, J. Eur. Ceram. Soc. **23** (2003) 1549.
[8] J. Töpfer, A. Feltz, D. Grãf, B. Hackl, L. Raupach, P. Weissbrodt, Phys. Stat. Sol. A **134** (1992) 405.
[9] S. Khademolhoseini, J. Mater. Sci. Mater. Electron. **28** (2017) 7899.
[10] R. Schmidt, A. Stiegelschmitt, A. Roosen, A.W. Brinkman, J. Eur. Ceram. Soc. **23** (2003) 1549.
[11] G. Ashcroft, I. Terry, R. Gover, J. Eur. Ceram. Soc. **26** (2006) 901.
[12] B.B. Nelson-Cheeseman, R.V. Chopdekar, J.M. Iwata, M.F. Toney, E. Arenholz, Y. Suzuki, Phys. Rev. B **82** (2010) 14419.
[13] H. Cui, M. Zayat, D. Levy, J. Sol-Gel Sci. Technol. **35** (2005) 175.
[14] R.M. Cornell, R. Giovanoli, Clays Clay Miner. **36** (1988) 249.
[15] Y. Li, X. Wang, Chem. Eur. J. **9** (2003) 300.
[16] W.-N. Li, Adv. Funct. Mater. **16**. (2006) 1247.
[17] X. Fu, J. Feng, H. Wang, K.M. Ng, Catal. Commun. **10** (2009) 1844.
[18] B.K. Mohapatra, B.R. Nayak, R.K. Sahoo, J. Min. Petr. Econ. Geol. **90** (1995) 280.
[19] M.K. Nimfopoulos, A.D. Pattrik, Mineral. Mag. **55** (1991) 423.
[20] K. Kuma, K. Usui, W. Paplawsky, B. Gedulin, G. Arrhenius. Mineral. Mag. **58** (1994) 425.

[21] K. Abou-El-Sherbini, M.H. Askar, R. Schorllon, Solid State Ion. **150** (2002) 407.
[22] C.M. Julien, M. Massot, C. Poisignon, Spectrochim. Acta A **60** (2004) 689.
[23] R.M. Potter, G.R. Robbman, Am. Mineral. **64** (1979) 1199.
[24] S. Åsbrink, A. Waskowska, J.S. Olsen, L. Gerward, Phys. Rev. B **57** (1998) 4972.
[25] L. Kang, M. Zhang, Z.-H. Liu, K. Ooi, Spectrochim. Acta A **67** (2007) 864.
[26] E.A. Johnson, E.J. Post, Am. Mineral. **91** (2006) 609.
[27] J. Jung, J. Töpfer, A. Feltz, J. Therm. Anal. Calorim. **36** (1990) 1505.
[28] M. Jha, J. Solid State Chem. **258** (2018) 722.
[29] S. Qiao, N. Huang, Y. Zhang, J. Zhang, Z. Gao, S. Zhou, Int. J. Hydrog. Energy **44** (2019) 18351.
[30] S.A. Dhas, J. Energy Storage **35** (2021) 10277.
[31] J.L.M. De Vidales, R.M. Rojas, E. Vila, O. Garcia-Martinez, Mater. Res. Bull. **29** (1994) 1163.
[32] A. Díez, R. Schimidt, A.E. Sagua, M.A. Frechero, E. Matesanz, C. Leon, E. Morán, J. Eur. Ceram. Soc. **30** (2010) 2617.
[33] S. Karmakar, C.D. Mistari, V. Parey, R. Thapa, M.A. More, D. Behera, J. Phys. D Appl. Phys. **53** (2020) 55103.
[34] A. Ray, A. Roy, M. Ghosh, J.A. Ramos-Ramón, S. Saha, U. Pal, S.K. Bhattacharya, S. Das, Appl. Surf. Sci. **463** (2019) 513.
[35] M.J. Abel, A. Pramothkumar, V. Archana, Res. Chem. Intermed. **46** (2020) 3509.
(Rec. 12/12/2022, Rev. 11/05/2023, Ac. 20/05/2023)